JOURNAL OF GEOPHYSICAL RESEARCH, VOL. 114, B05303, doi:10.1029/2008JB005873, 2009

Direct measures of lateral velocity variation in the deep Earth

Daoyuan Sun,[1] Don Helmberger,[1] Sidao Ni,[2] and Dan Bower[1]

Received 14 June 2008; revised 2 January 2009; accepted 17 March 2009; published 19 May 2009.

[1] Current tomographic models of the Earth display perturbations to a radial stratified reference model. However, structures in the deep mantle that are chemically dense with low Rayleigh numbers can develop enormous relief, perhaps with boundaries closer to vertical than to radial. Such features are hard to detect with present tomographic modeling techniques because the timing anomalies are based on long-period filtered waveforms with complexity removed. Here we develop a new tool for processing array data on the basis of a decomposition referred to as a multipath detector, which can be used to distinguish between horizontal structure (in-plane multipathing) and vertical (out-of-plane multipathing) directly from processing array waveforms. A lateral gradient coefficient based on this detector provides a direct constraint on the sharpness of the boundaries and material properties. We demonstrate the usefulness of this approach by processing samples of both *P* and *S* data from the Kaapvaal array in southern Africa, which are compared with synthetic predictions from a metastable dynamic model containing sharp edges. Both data and simulations produce timing gradients larger than 2 s/deg in azimuthal changes for *S* waves, where only minor effects are obtained for *P* waves. These results further validate the case for distinct chemistry inside the African Low Shear Velocity Province.

Citation: Sun, D., D. Helmberger, S. Ni, and D. Bower (2009), Direct measures of lateral velocity variation in the deep Earth, *J. Geophys. Res.*, *114*, B05303, doi:10.1029/2008JB005873.

1. Introduction

[2] The upper mantle and crust display strong stratification apparently caused by mineral density differentiation. Record sections of upper mantle triplications indicate discontinuities in seismic velocity jumps at depths near 410 and 660 km depth in both *P* and *S* velocity [e.g., *Grand and Helmberger*, 1984]. These features have been studied globally [*Shearer*, 1993] and are well accepted supporting a radial stratified mantle. However, *Masters et al.* [2000] argue for less uniformity in *P* and *S* velocity compatibility in the lower mantle, leading *Anderson* [2002] to speculate on chemically based structure. He concludes that such a layer would have high conductivity and viscosity but very low thermal expansivity (small thermal buoyancy). Thus, in contrast to conditions in the upper mantle, dynamically generated features in the lower mantle are predicted to be sluggish, long-lived, and perhaps develop enormous relief [*Davaille*, 1999; *Gonnermann et al.*, 2002; *Gurnis et al.*, 1998; *Hansen and Yuen*, 1989; *Kellogg et al.*, 1999; *Tackley*, 2000; *Tan and Gurnis*, 2005, 2007].

[3] We can test for these types of predictions by searching for sharp velocity gradients, which may be oriented more vertically than horizontally. One method to achieve this is to examine how wavefronts arrive at broadband two-dimensional arrays such as the Kaapvaal array in southern Africa as displayed in Figure 1. The various traces contain the diffracted SH phases sampling produced by two deep earthquakes: one in the western Pacific (A) and one beneath South America (B). The record sections in Figure 1 are plotted with respect to the travel time predictions from the preliminary reference Earth model (PREM) [*Dziewonski and Anderson*, 1981]. That is, each record is shifted in time for a distance correction such that it should be perfectly aligned along the reference line at position zero if the Earth is adequately modeled by PREM. An example of a record section for event A plotted as a function of distance is given in Figure 1b, and that in azimuth is given in Figure 1c, a so-called "fan shot." The latter presentation is a common oil exploration tool to detect salt domes. The plot of event A in azimuth (Figure 1c) shows more order, with uniform behavior from trace-to-trace in timing and shape. Thus we suggest that the structure is varying more in azimuth than in distance and that the structure is oriented more vertically than radially. We have included a set of heavy lines in the azimuthal plots for event A (Figure 1c) to indicate pulses associated with distinct paths. The first heavy line in Figure 1c corresponds to relatively fast paths that avoid the slow structure by taking a northerly route. The second heavy line denotes delayed signals following slow paths sampling inside the structure. Such complexity or multipathing is expected for rapidly varying structures and can be modeled accordingly [*Ni et al.*, 2005].

[4] While the *S* waves display strong azimuthal patterns, the *P* waves remain PREM-like as displayed in Figure 1d. The events examined in this study and other recent reports

[1] Seismological Laboratory, California Institute of Technology, Pasadena, California, USA.
[2] URS, Inc., Pasadena, California, USA.

0148-0227/09/2008JB005873$09.00

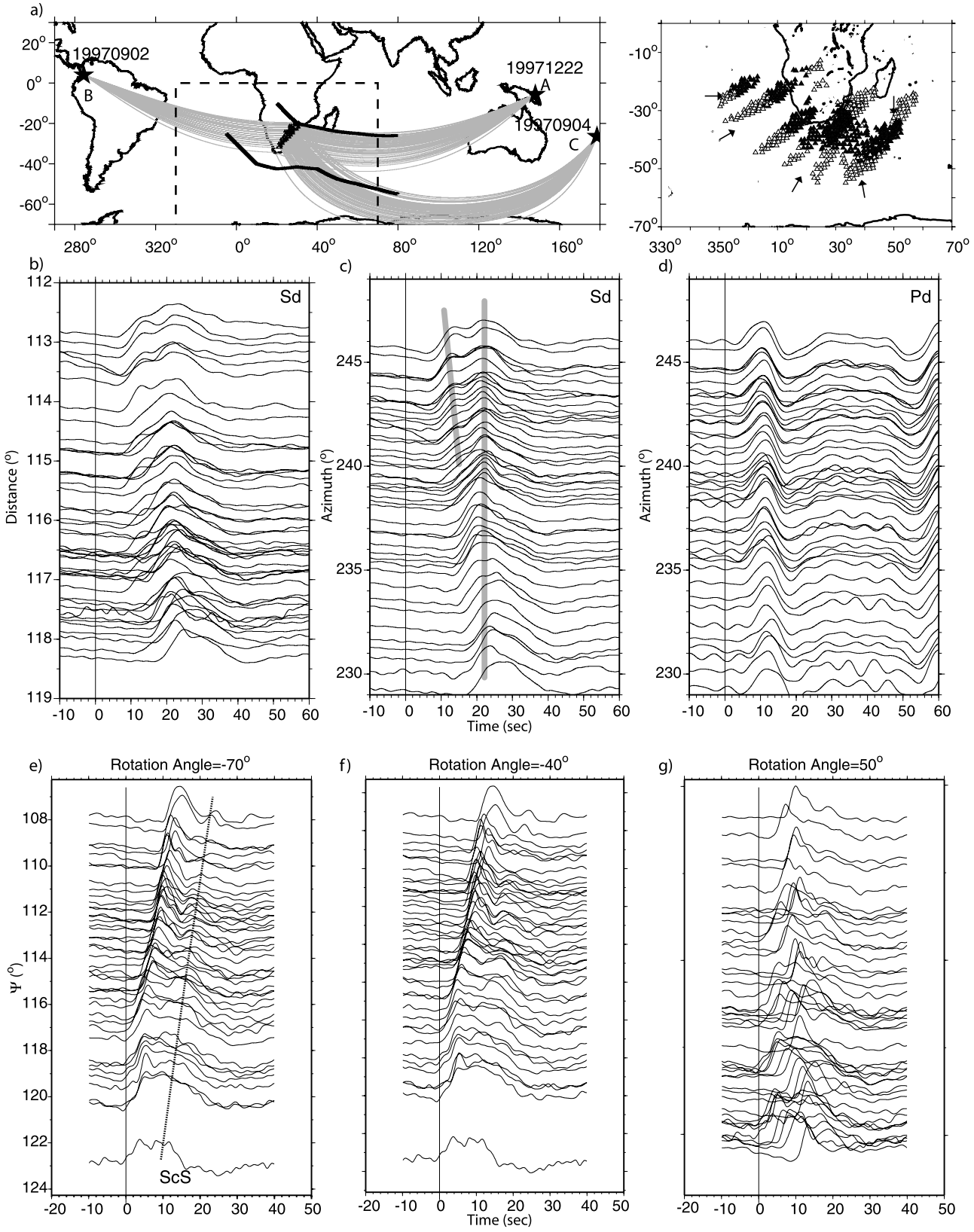
a)
19970902
B
19971222
A
19970904
C
b)
Sd
Distance (°)
c)
Sd
Azimuth (°)
d)
Pd
Azimuth (°)
Time (sec)
e)
Rotation Angle=-70°
Ψ (°)
ScS
f)
Rotation Angle=-40°
Time (sec)
g)
Rotation Angle=50°

Figure 1

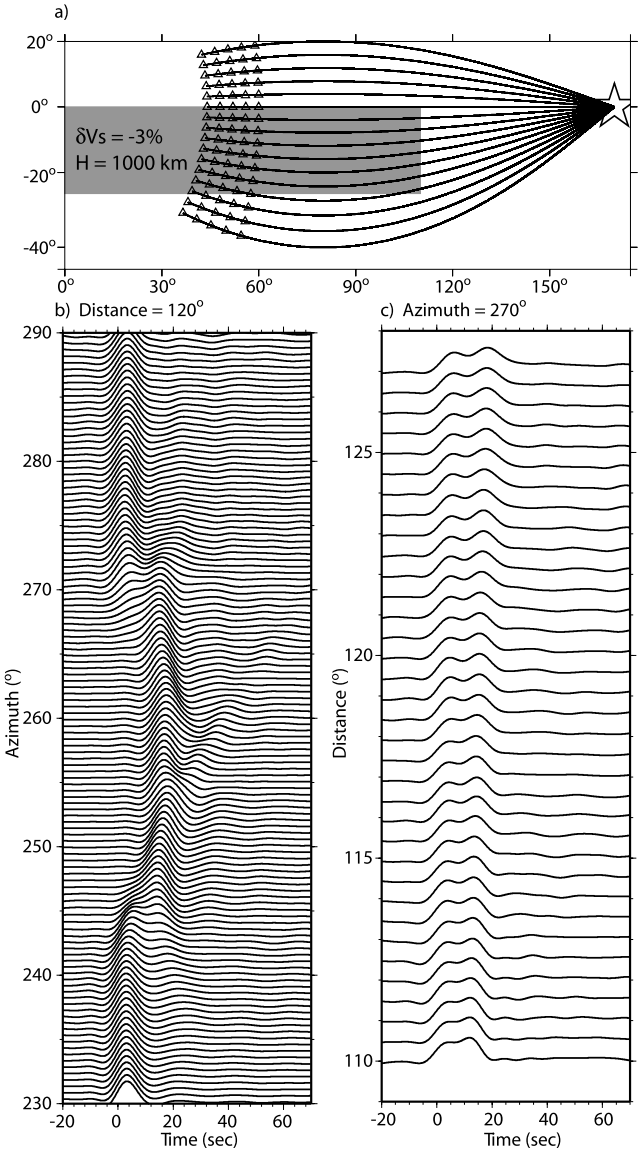

Figure 2. Synthetic seismograms generated by spectral-element method (SEM) for the model along with source-station geometry. (a) The model. (b) Fan shot at a constant distance of 112°. (c) A record section in distance appropriate for an azimuth of 270°.

do not show many recognizable *P* wave anomalies [*Wen*, 2001; *Ni and Helmberger*, 2003a, 2003b, 2003c]. The uniformity of the *P* waves suggests neglectable upper mantle variation beneath the stations, which is in agreement with the studies by *James et al.* [2001]. Moreover, since we are analyzing the same event, we are avoiding the many problems concerning records assembled from multiple earthquakes, such as individual source excitations, uncertain locations, and origin times, which tend to smooth tomographic images.

[5] *SKS* raypaths from the southwest encounter the structure at right angles to the anomalous structure where the delay can be seen directly, varying roughly 6 s over a distance of a few degrees (Figure 1a). Such time delays are measured by cross correlation and delays relative to PREM projected along the raypaths to their core-mantle boundary (CMB) exit points as displayed; see the work of *Helmberger and Ni* [2005a] for details. Note the sharp jump from distinct boundaries which delineate a broad structure changing from a northwestern orientation to east-west below South Africa.

[6] The delay gradient can also be seen directly in seismic sections as displayed in Figure 1e, where raypaths approaching the array from the west sample the structural boundary at an angle so that the wavefront is not perpendicular to the great circle path. To estimate this angle (θ), we simply perform a grid search of distance-azimuth combinations or ψ = distance · sin θ + azimuth · cos θ until we find the most orderly section in waveform shape and timing. The angle is measured relative to the true azimuth so that $\pm 90^\circ$ corresponds to a normal distance section and 0° to pure azimuthal plot as given in Figure 1c. An example of a mixture in distance and azimuth is given in Figures 1e–1g. Note that the upper group of records for event B prefers a -70° approach, while -40° fits the lower half better. This indicates the gradual changes to east-west for the southernmost portion of the array. We have included a northeast orientation (50°) that shows the most disorder for comparison (Figure 1g).

[7] The waveform data recorded by the array from the various sources have been processed to estimate their preferred delay gradient directions indicated by arrows with the results included in Figure 1a. The general pattern is quite clear with the arrows consistently pointing toward the middle of the structure. The same pattern is produced by the *SKS* and *SKKS* delays, which is based solely on relative timing [*Ni and Helmberger*, 2003c]. However, some of these *SKS* appear to be multipathed which occurs along the boundaries. Many of the observations recorded by the Kaapvaal array have been modeled following two distinct strategies: one involving pure two-dimensional (2-D) modeling (in-plane, Figure 1b) [*Wang and Wen*, 2007], and the other involving azimuthal multipathing (out-of-plane, Figure 1c) modeling [*Ni et al.*, 2005]. An earlier effort by *Wen* [2001] produced an excellent fit to individual records, where the data in Figure 1c (event A, 22 December 1997) are broken into sectors of azimuth and modeled with a hybrid numerical formalism. In this case, the large second arrival is actually a delayed *ScS* produced by a very slow basal layer ($\delta V_s = -12\%$). The second arrival can also be

Figure 1. Display of event paths and observations from the Kaapvaal array. (a) Locations of three deep earthquakes and their great circle paths to the array (left map) and a blowup of a pattern of *SKS-SKKS* delays (exit points at the core-mantle boundary, CMB) associated with the boundary of the African superplume (right map). Delays of more than 5 s are shown in solid triangles. Open triangles indicate no delay. The black solid line in Figure 1a indicates the approximate position of the African superplume. (b) S_d data from event A, plotted with distance (record section). (c) S_d data from event A, with azimuth (fan shot). (d) P_d data. (e–g) Waveform data from event B plotted as a function of ψ, a combination of distance and azimuth as addressed in the text.

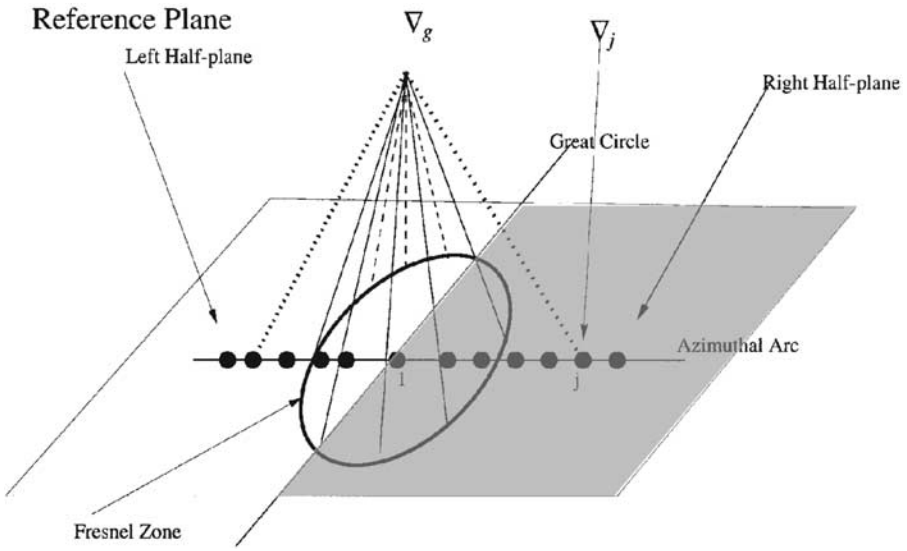

Figure 3. Construction of a reference plane directly above an edge, displayed where the great circle is along the edge. The Fresnel zone is indicated as a circle with half above the slow zone (right side, shaded) and half normal (left side). We have included a line of samples along an azimuthal arc, where a two-dimensional (2-D) summation over the plane is replaced with a line integration.

produced by an out-of-plane arrival. Thus the interpretations of the two approaches produce different models. These two models have distinctly different physical interpretations as well. Gently sloping walls over a very low velocity basal layer favors "stable piles" [*McNamara and Zhong*, 2004], while more vertical walls with more uniform internal structure favors the "metastable" type interpretation proposed by *Tan and Gurnis* [2005]. Thus, to address these important issues, we will introduce a new method of using array data such as that in Figure 1, to address in-plane versus out-of-plane propagational features directly. The method relies on the organization of the waveform complexity with the relative timing between arrivals as a function of position. We introduce the approach with a review of a hybrid method of generating 3-D synthetics, which suggests that out-of-plane arrivals can be simulated by using diffraction operators. Each observation is then approximated by four arrivals which sample the extended Fresnel zone. The array of observations is then replaced by a footprint of timing shifts between interfering arrivals. To interpret these maps, we present a set of training exercises on synthetics to develop a multipath detector (MPD) scheme that uses the gradient in differential arrivals to determine in-plane versus out-of-plane patterns. Then we apply MPD on two real data profiles to demonstrate the sharp edges of the African superplume.

2. Methodology

[8] Dense arrays as discussed above, are displaying obvious waveform complexities, which makes travel time picking difficult. The usual solution adopted in tomography is to low-pass filter until the waveforms are similar enough to cross correlate [*Masters et al.*, 2000] or pick the first arrival. Here we will introduce a new approach that uses more of the waveform complexity to infer the presence of sharp boundaries. We will begin with a numerical simulation of a simple block model with sharp walls followed by a brief review of a recent technique developed to treat 3-D structure. To illustrate azimuthal multipathing, we generate synthetics for a uniform low-velocity structure (LVS) embedded in PREM displayed in Figure 2 using the 3-D spectral-element method (SEM) [*Komatitsch and Tromp*, 2002a, 2002b]. The synthetics were generated on a fine grid showing the effects of paths crossing the sharp wall with two record sections displayed: one as a function of azimuth (Figure 2c) and another a normal function of distance record section (Figure 2b). For azimuths near 270°, two arrivals of nearly the same amplitude are apparent with one lagged by about 10 s, corresponding to the slow path inside the LVS. A similar pattern can be seen along the other wall near 245°. The first arrival times produce a simple pattern (Figure 2a on right) indicating the delayed patch of arrivals with a transition zone given along the edge which we want to explore in terms of developing a new tomographic approach. In particular, we address a method of characterizing the waveform distortion such as displayed in Figure 2 in a relatively simple manner in preparation for constructing a seismic model using raypaths as presented by *Zhu and Helmberger* [1998].

[9] One useful approach in treating such problems is to introduce a reference plane and use Huygen's principle. Suppose we place such a plane above the box and examine the arrivals along the edge where a great circle path is located (Figure 3). A solution can then be generated by summing over paths connecting every point on a 3-D grid to the source and receiver [i.e., *Scott and Helmberger*, 1985]. An exact solution can be generated in this way as demonstrated by *Helmberger and Ni* [2005b]. Fortunately, we can reduce this 3-D summation to an integration along a line as indicated in Figure 3 and still further to the summation of just four responses by applying a sequence of approximations. Thus we start with a brief review of

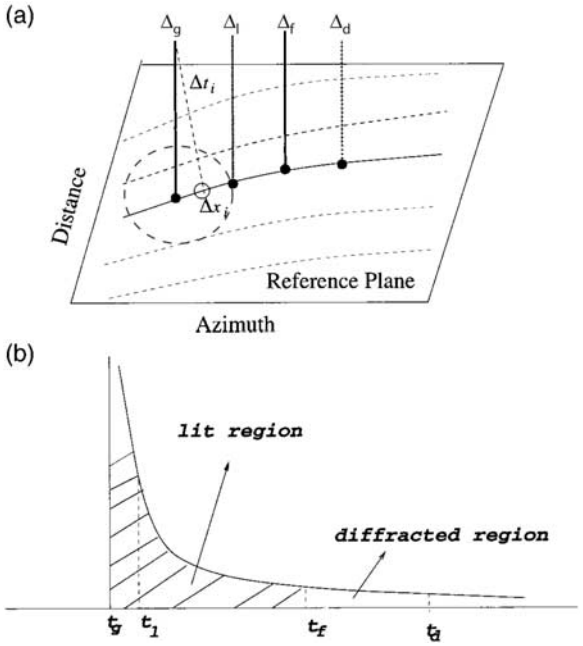

Figure 4. Presentation of a simplified Kirchhoff secondary-source summation procedure. (a) Reference surface positioned above a 3-D target structure, where we replace a grid summation with an approximate solution. Four locations are indicated, corresponding to projections to the surface: Δ_g, the geometric path; Δ_l, a sample of the lit region; Δ_f, the Fresnel zone limit; and Δ_d, a sample of the diffracted contribution. The dotted lines represent paths of constant distance. (b) The $1/\sqrt{t}$ convolution operator, with t_1 indicating the half-area position under the curve approximation, which ends at t_f (similarly, t_d from t_f to ∞).

generating approximate synthetics for testing against those displayed in Figure 2.

2.1. Brief Review of Approximate Methods

[10] A well-known technique for generating 1-D synthetics was introduced by *Chapman* [1976], called the WKBJ method. The displacement wavefield can be written as

$$V(r,z,t) = \frac{d}{dt}\left[\dot{D}(t) * \frac{1}{\sqrt{t}} * G^2(r,z,t)\right], \tag{1}$$

where $\dot{D}(t)$ is the far-field time history of a simple shear dislocation. G^2 is a 1-D or 2-D Green's function where the model has no azimuthal dependence,

$$G^2(r,z,t) = \sqrt{\frac{2}{r}}\frac{1}{\pi}\psi(r,z,t), \tag{2}$$

and r is the radial distance along an Earth-flattened model, with z as the vertical coordinate and ψ (r, z, t) as the line source solution [*Chapman*, 2004]. The operator $(1/\sqrt{t})$ and the $(1/\sqrt{r})$ essentially correct for the distance dependence in 2-D propagation and extra amplitude decay associated with 3-D spreading. The function ψ (r, z, t) relates the ray parameter (p_i) to the travel times (t_i) for a family of paths arriving near the receiver. The WKBJ amplitudes can be approximated by

$$\psi(r,z,t) \approx \sum\left(\frac{\delta p_i}{\delta t_i}\right), \tag{3}$$

where (δ) measures the differences between neighboring paths. For smooth velocity structures, δt_i approaches zero at the first arrival (t_o), and

$$\psi(r,z,t) \approx \frac{H(t-t_0)}{\sqrt{t-t_0}}. \tag{4}$$

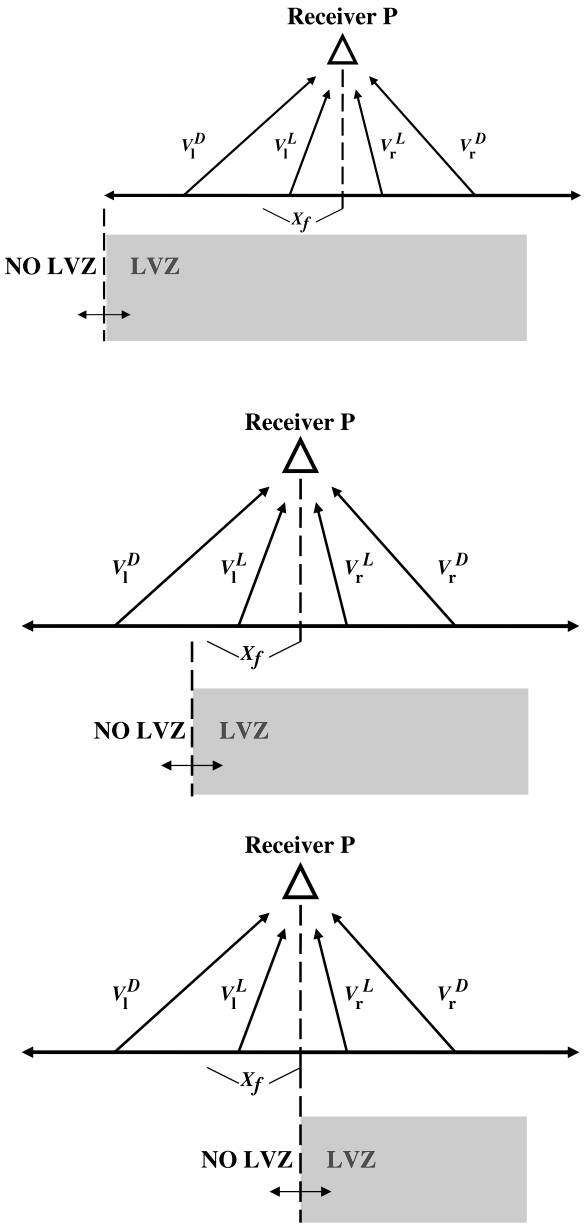

Figure 5. Cartoon displaying the sampling of low-velocity zone (LVZ, shaded) versus normal (not shaded) at right angles to the great circle path with four contributions: two lit V_r^L and V_l^L and two diffracted V_r^D and V_l^D. Note that the long-period diffractions can be early, as in the middle cartoon, or late, as the receiver moves to the right.

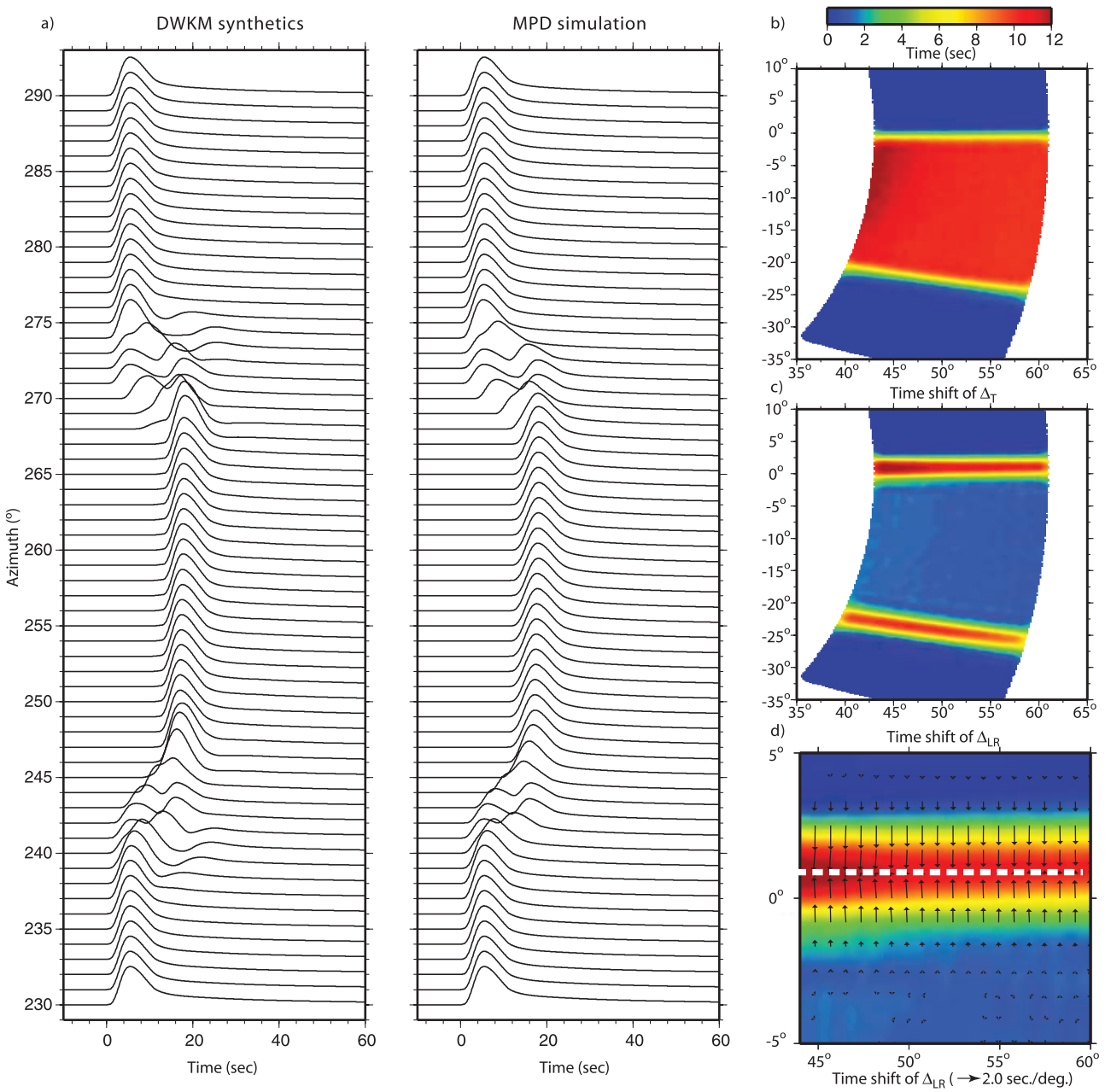

Figure 6. Synthetic training exercise with the problem setup displayed in Figure 2a used in the SEM simulation. (a) A comparison of 3-D synthetics (DWKM method) and multipath detector (MPD) results. (b–d) Large array time delays. The results are color-coded. The edge structures are highlighted with white dashed lines in Figure 6d.

As discussed in box 9.8 of *Aki and Richards* [2002], equation (1) becomes

$$V \approx \frac{d}{dt}\left[\dot{D}(t) * \frac{1}{\sqrt{t}} * \frac{H(t-t_0)}{\sqrt{t-t_0}}\right] \cong \dot{D}\,(t - t_o), \qquad (5)$$

where $\dot{D}$ is the source time function.

[11] Note that the $(1/\sqrt{t})$ operator was obtained by assuming axial symmetry. Thus, in situations such as Figure 3, the arrivals from left to right vary in azimuth but remain weighted by their distance from the geometric great circle path (Δ_g). Thus geometry plays an essential role, and the sampling in azimuth becomes similar to (δp_i) in the radial distance with points nearest Δ_g contributing relative to a square-root singularity as indicated in Figure 4. We can simplify this convolution operator by assuming $\psi\,(r, z, t)$ is slowly varying relative to $1/\sqrt{t - t_o}$ near $t = t_o$ and compute ψ at four locations controlled by the Fresnel zone. We define its radius to be

$$\Delta_f = \sqrt{\delta_\alpha^2 t_e T}, \qquad (6)$$

where t_e is the differential travel time to the feature causing the complexity, δ_α is the average velocity, and T is the

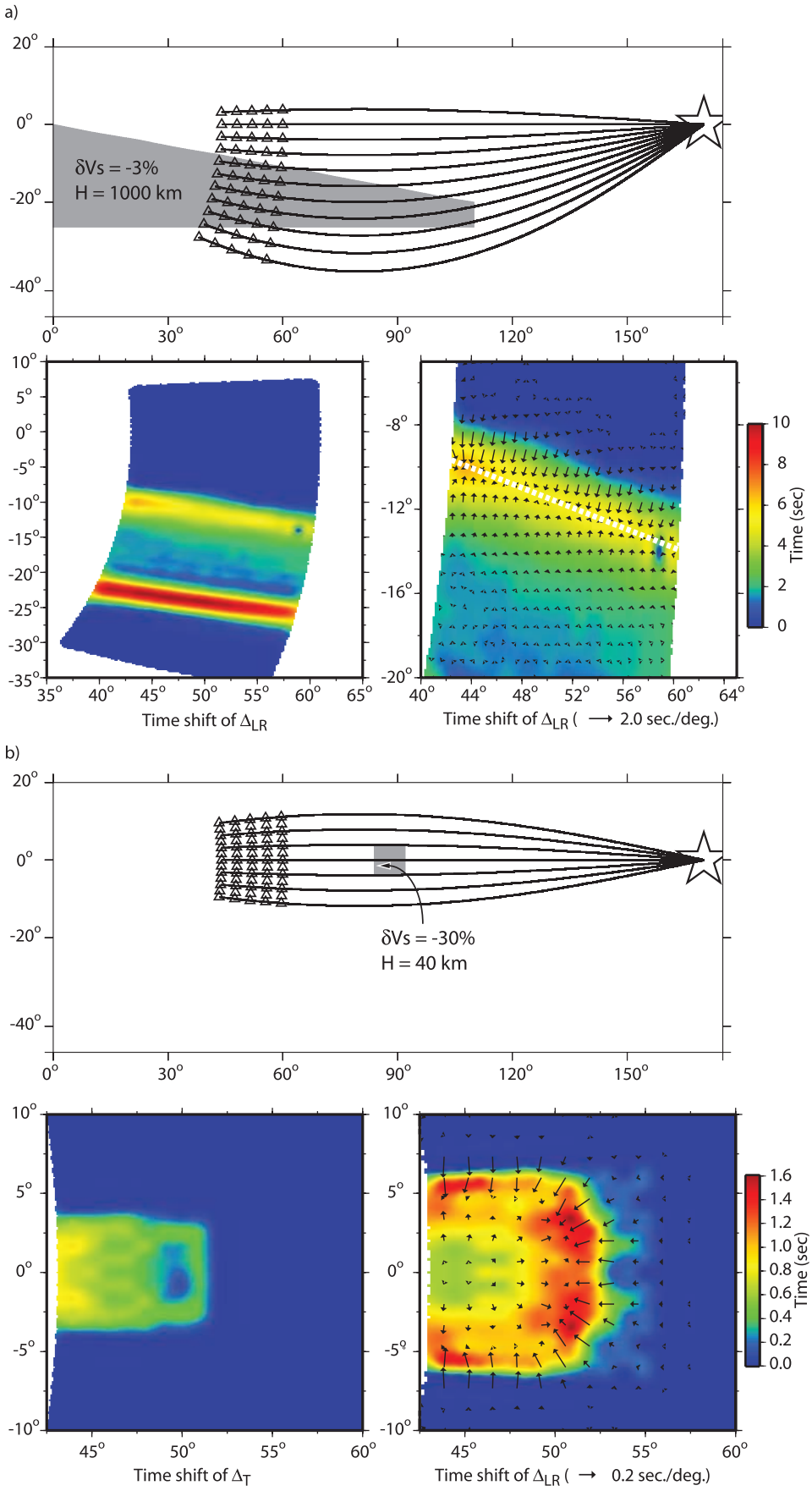

Figure 7. Synthetic training exercise for more complex structures containing (a) a "tapered ended" large low-velocity province and (b) an ultralow-velocity zone (ULVZ) sample.

source duration. We then compute ψ (r, z, t) at Δ_l and Δ_d defined by

$$\Delta_l = \sqrt{\delta_\alpha^2 t_e T/4}, \qquad \Delta_d = \left(\sqrt{2}+1\right)\Delta_l, \tag{7}$$

corresponding to the lit and diffraction zone. Next, we assume the seismic model is smoothly varying above the reference plane and compute ψ at the surface. Adding Δ will produce a broadband response as in adding raypaths in WKBJ theory; see the work of *Helmberger and Ni* [2005b] for details. Thus, to approximate non–great circle path contributions, we generate

$$V(r,z,t) = O_L * G_R^2(\Delta_l) + O_D * G_R^2(\Delta_d) + O_L * G_L^2(\Delta_l) + O_D * G_L^2(\Delta_d), \tag{8}$$

assuming that the right side and left side have distinct responses at Δ_l and Δ_d on each side. The operators are weighted by their distance away from Δ_f with t_f the extra time taken to travel to the Fresnel edge, or

$$O_L = \frac{d}{dt}\left[\left(\frac{H(t)}{\sqrt{t}} - \frac{H(t-t_f)}{\sqrt{t}}\right) * \dot{D}(t)\right],$$
$$O_D = \frac{d}{dt}\left[\frac{H(t-t_f)}{\sqrt{t}} * \dot{D}(t)\right]. \tag{9}$$

Figure 5 displays a diagram indicating the simulation relative to the boundary, and Figure 6 presents the synthetics generated from the application of equation (8), which is referred to as the DWKM method by *Helmberger and Ni* [2005b]. All four responses sample the box at azimuths 250°–265°. At 268°, one sample, Δ_d on the left, encounters the faster velocity and arrives early. Note its longer-period nature. Directly above the edge, two early and two late arrivals interfere. Note that these synthetics compare well with those given in Figure 2 for wall crossings. In this zone, the relative timing differential between the right and left is the most obvious and can be used to generate the new tool, namely, the multipath detector (MPD). If we focus on short periods, we can greatly simplify the procedure and treat only the left and right aspects of the field:

$$V(t) = O * G_R^2(\Delta_l) + O * G_L^2(\Delta_l), \tag{10}$$

where

$$O(t) = \frac{d}{dt}\left[\frac{1}{\sqrt{t}} * \dot{D}(t)\right], \tag{11}$$

which becomes the point-source solution. A common practice in modeling a triplication is to pick a simple pulse

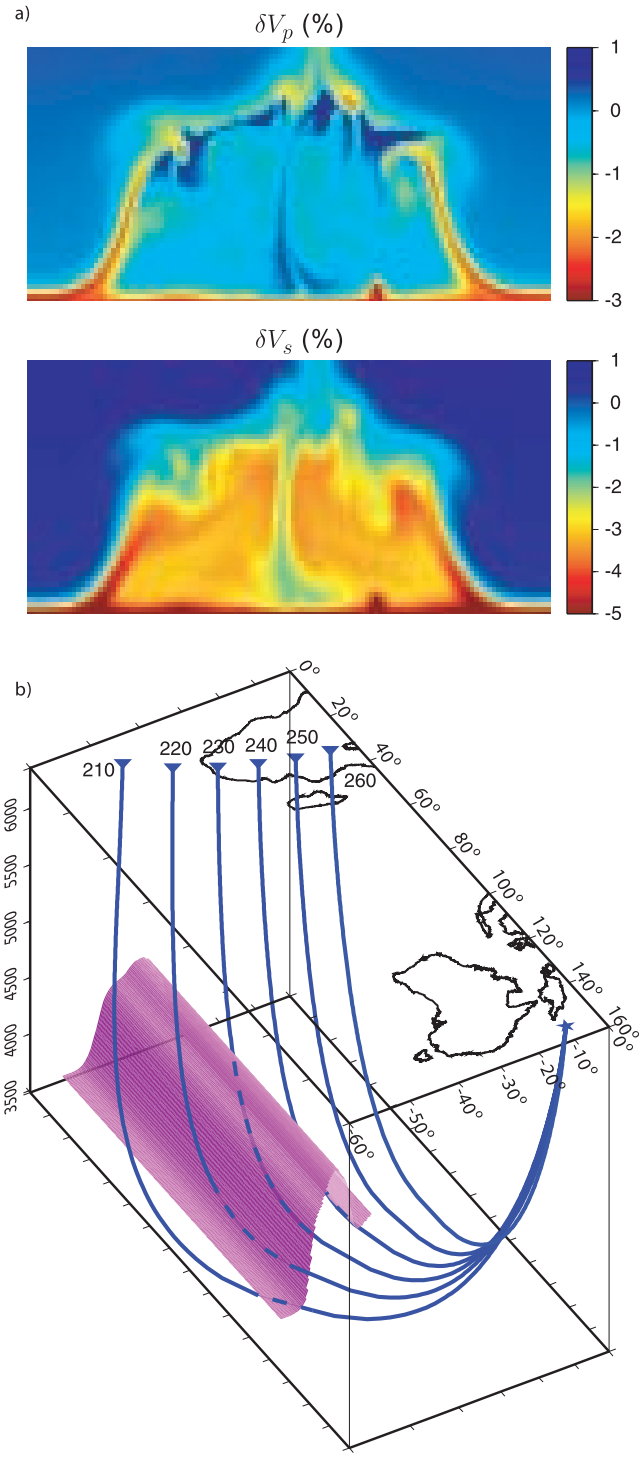

Figure 8. (a) A 2-D section through a metastable thermochemical structure with δV_p and δV_s. The average percentage drop is 3% for V_s and less than 1% for V_p. The structure is 1000 km high and 1500 km wide. Note the plumes along the edges, which are wider and shifted internally for S relative to P [see *Tan and Gurnis*, 2005]. (b) Raypaths traveling from a source beneath Fiji-Tonga to an imaginary array (triangles) at various azimuths but constant distance (fan shot) encountering a 3-D structure containing 2-D slices of metastable superplume model represented by the purple ridge. The ridge structure is aligned roughly with the northern edge as given in Figure 1. We assume the ends are truncated as displayed and obviously represent a greatly simplified structure. Paths at 250° and 210° miss the structure and are preliminary reference Earth model–like (PREM-like).

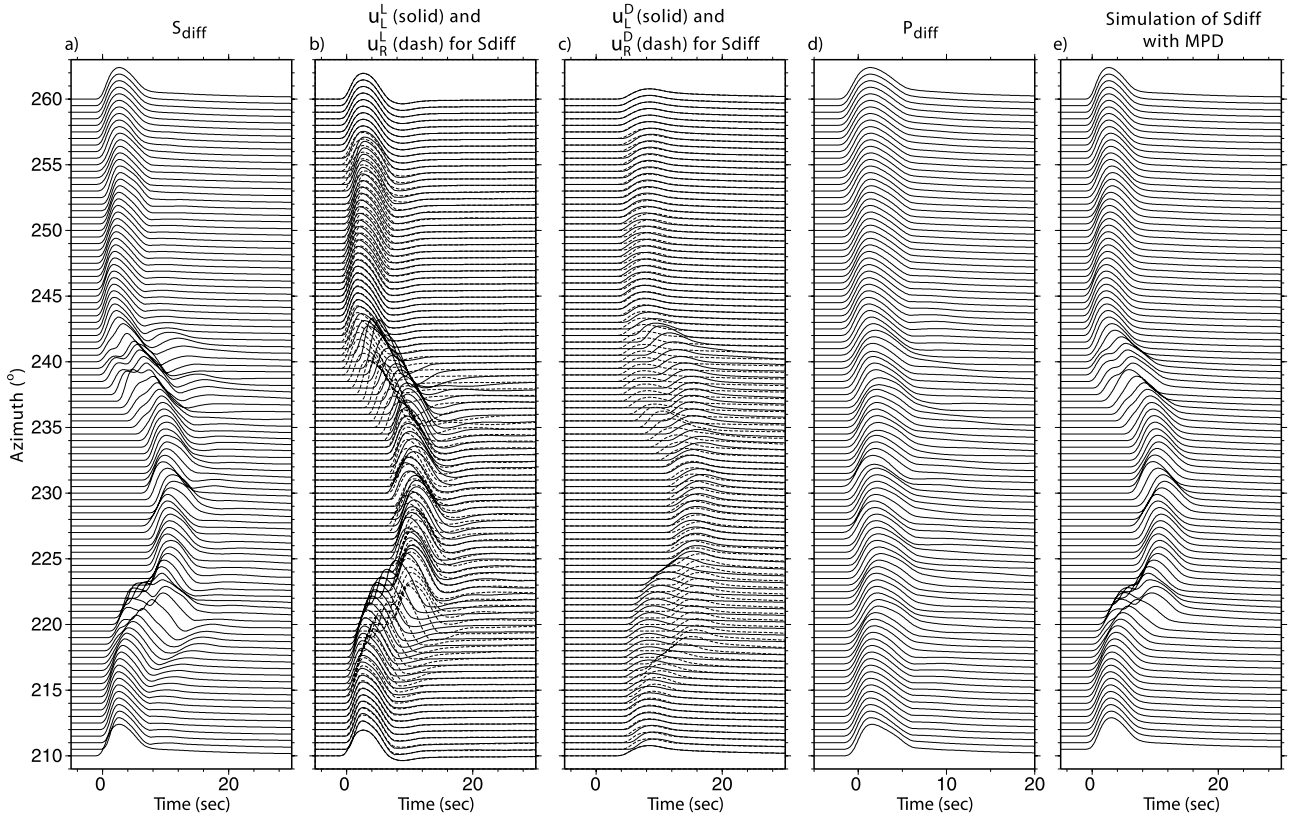

Figure 9. (a) Construction of approximate 3-D synthetics for S_d at constant distance ($\Delta = 110°$). (b, c) The "lit" and "diffracted" contributions. (d) P_d, which is much less dramatic but also sensitive to internal structure. (e) Simulation by simple construction with MPD discussed in the text.

from a forward branch and assume it is $\dot{D}$(t), or empirical source history [*Gilbert and Helmberger*, 1972]. Thus we assume that any observation is constructed from $O(t)$ (equation (10)) but split by some δt, which is obvious in Figure 6. We can then determine the timing shift and reference beginning time by direct grid search of each seismogram. This approach generated the simulations in Figure 6. Note that we lose the diffracted tails but still pick up the edges very well. We recover two timing delays. One associated with the shift between the left and the right branches (Δ_{LR}), and the other between the entire simulation relative to the reference model or total delay (Δ_T). The differential times generated from a 2-D array can then be used to construct the spatial gradient of these delays as displayed in Figure 6b. These correspond to the two wall crossovers, which are slightly different because of the geometry. The arrows perpendicular with the radial direction suggests the waveform distortions are caused by out-of-plane multipathing. Note that the vectors change sign at the maximum in shift, denoted by a heavy, white dotted line, which indicates the edge of the structure is parallel with the radial direction. For the structure in Figure 7a, which incorporates a tapered end, the "zero-gradient" line crosses the radial direction at an angle (Figure 7a). The analyses, again, retrieves the angle between the edge of the structure and the radial direction. Synthetics from an idealized ultralow-velocity zone (ULVZ) structure are given in Figure 7b. Note that the arrows become parallel with the radial direction indicating that this structure will cause mostly radial direction multipathing (in-plane). Thus the footprints generated with the MPD analysis of array data can be used directly to determine if the edges of a structure are in-plane or out-of-plane. These examples are highly idealized and the issue of applicability to more complex structures needs to be addressed. For such a demonstration, we chose a dynamic model for the African plume since it produces synthetics with features similar to the observations in Figure 1.

2.2. Metastable Structures

[12] If the intrinsic density $\Delta\rho_{ch}$ is depth-dependent and changes with depth faster than the thermal density ($\Delta\rho_{th}$), it is possible to generate metastable structures as displayed in Figure 8. The V_p and V_s images are predictions from a material with a larger bulk modulus (6%) than the ambient mantle and higher zero pressure density (2.25%) [*Tan and Gurnis*, 2005]. The layer forms a single dynamic structure with a nearly neutral average density. Note the plumes along the edges and the downwelling near the middle. The parameters chosen in this particular model were an attempt to explain a simplified 2-D structure beneath South Africa, proposed by *Ni and Helmberger* [2003a, 2003b, 2003c] and *Wang and Wen* [2007]. *Sun et al.* [2007] inserted this structure into tomographic models and validated its usefulness in explaining 2-D seismic waveform data. The model in Figure 8a predicts more complexity at the edges than embedded in the simple block structure by *Ni et al.* [2005] and looks more like that proposed by *Wang and Wen* [2007]. However, the small-scale convection inside the

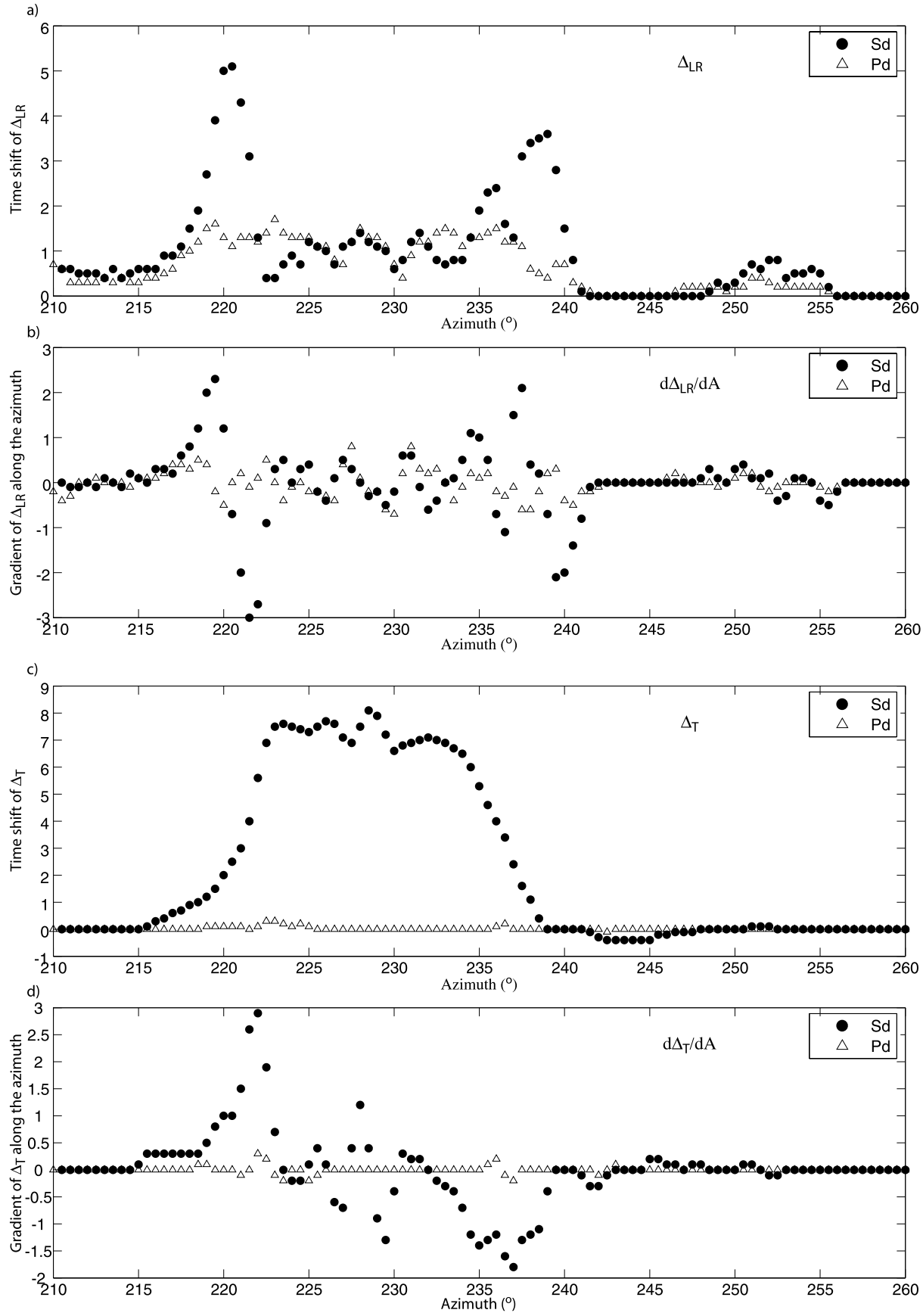

Figure 10. Presentation of timing delays and their azimuthal derivatives (d/dA). (a) Timing shift between the left side relative to the right (Δ_{LR}). (b) Azimuthal derivative $\Delta_{LR}(d\Delta_{LR}/dA)$. (c, d) The total shift of each trace relative to the reference model (PREM) and the derivative.

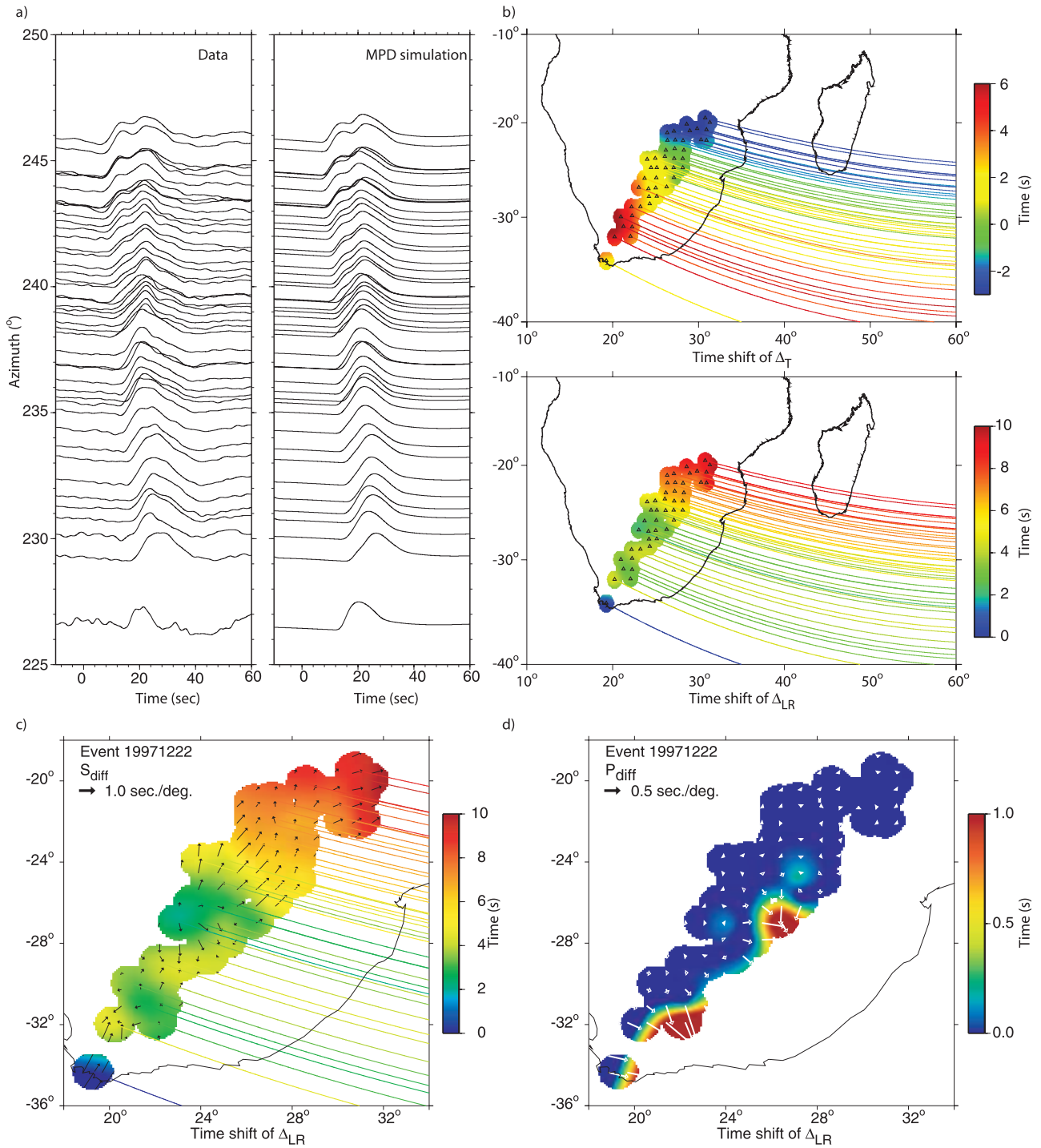

Figure 11. (a) The observations for event A (22 December 1997) of Figure 1 along with the MPD results. (b) The travel time shifts corresponding to Figure 11a. The blue paths are fast relative to the red paths. The differential shifts (Δ_{LR}) reach 10 s offsets near the top. (c, d) Detailed comparison between the *P* and *S* results.

structure changes with time, and its 3-D structure is probably extremely complicated since it must be influenced by the large-scale convection produced by global 3-D plate history. Such structures are presently being investigated [i.e., *Bunge et al.*, 2003]. Here we produce a 3-D structure by extending the 2-D metastable superplume model into an elongated structure with truncated ends. The 3-D synthetics for a "fan shot" are calculated for both S_{diff} (Figure 9a) and P_{diff} (Figure 9d). The synthetics are generated with the DWKM code discussed above. Partial responses are given in Figures 9b and 9c. For S_{diff}, the waveforms are strongly distorted when the rays travel across the boundaries (around 222° and 239°). Note the simplicity of P_{diff} relative to S_{diff} as expected from the 2-D velocity sections, since the

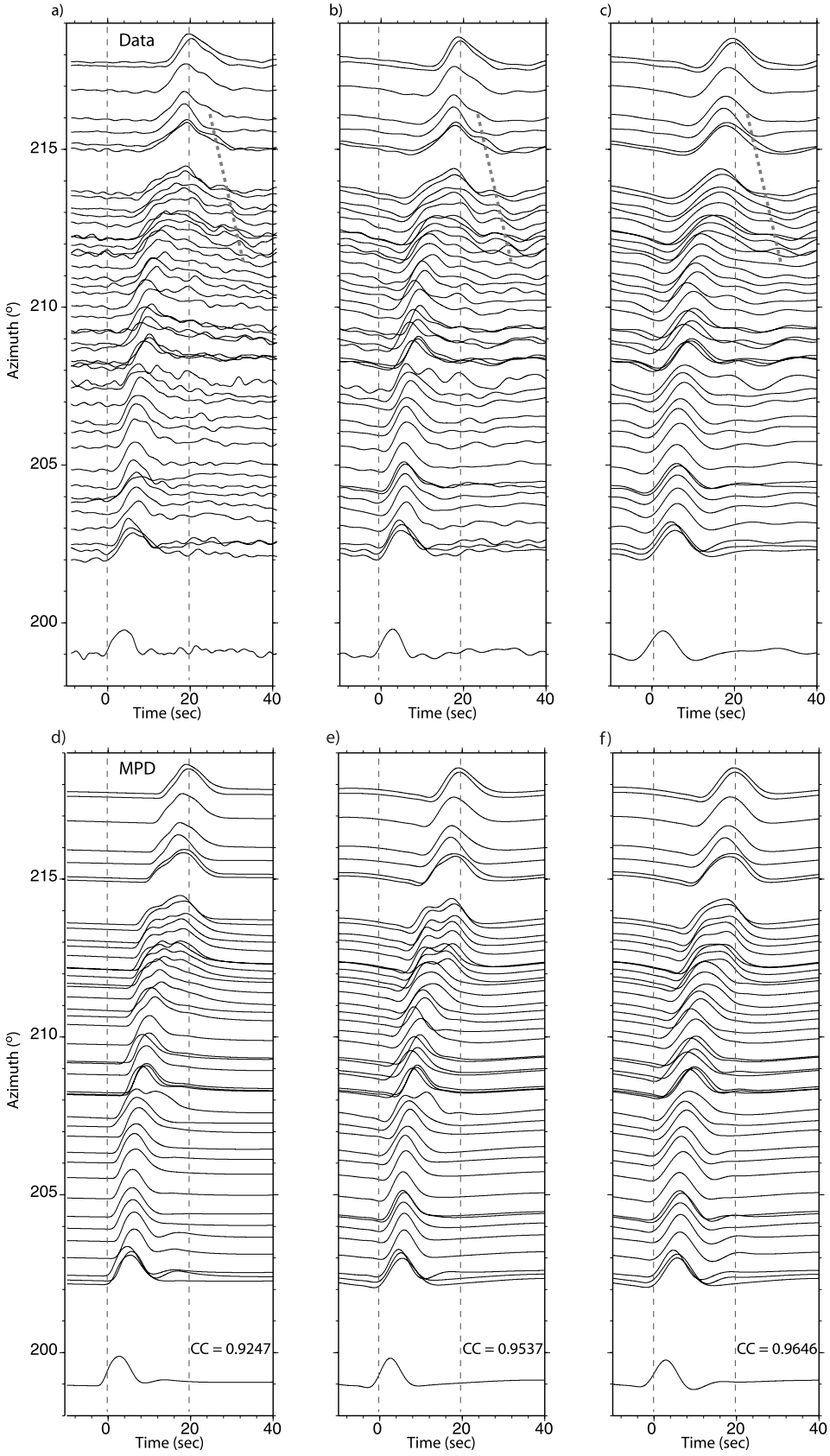

Figure 12. Application of the MPD analyses to event C (4 September 1997) (paths in Figure 1) as a function of frequency with (a, d) broadband (BB), (b, e) filtered to longer than 5 s, and (c, f) filtered to longer than 10 s. Figures 12a–12c contain the data, with the MPD results given in Figures 12d–12f. Note that the fits remain high even at BB periods, with cross-correlation coefficient of ~0.93.

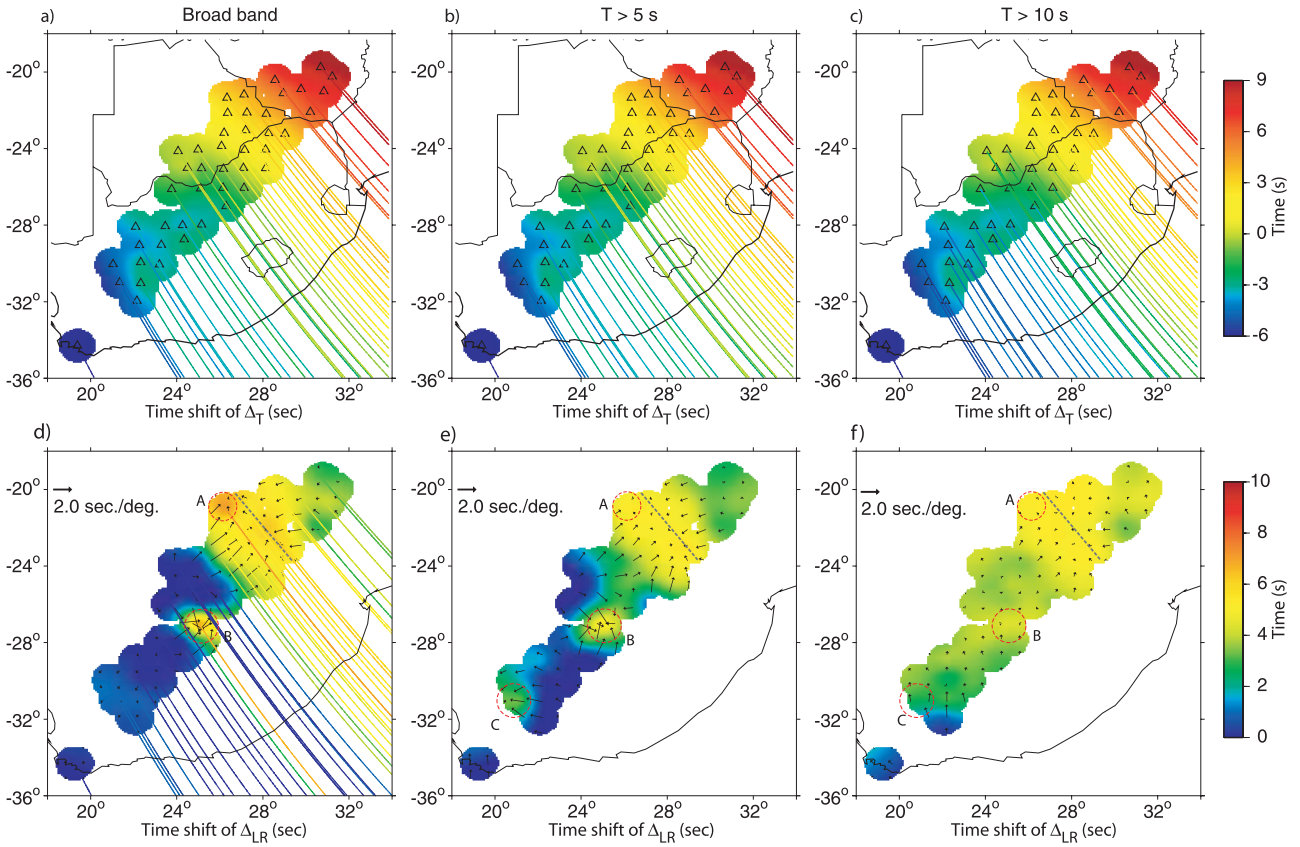

Figure 13. Delay time results for data (S_d) of Figure 12 with different frequency bands for (a–c) Δ_T and (d–f) Δ_{LR}. We have included the gradient of Δ_{LR} as arrows that display the wall-crossing position indicated by the heavy dashed line. Some small-scale structures occur near the wall (circle A) and to the west (circle B), which have the footprint of ULVZs.

velocity anomaly is relatively small in Figure 8a for (δV_p) relative to δV_s. The components (Figures 9b and 9c) suggest that the complex waveforms are caused by the large differential times between branches sampling the various paths, as in the earlier examples. The longer the period, the greater the reach, and at long enough periods the structure disappears. Obviously, the shorter periods are the most useful in defining the edges so that working at the shortest periods possible is the most diagnostic.

[13] Figure 9e displays the MPD analysis for *S* waves, and although it neglects the longer-period diffractions, it captures the essential edge structure. A more detailed description of the timing measurements is given in Figure 10 for both the *P* and *S* waves. First, we measure Δ_{LR} the shift parameter and its spatial gradient given in Figure 10b. The two zones of interference are especially strong in *S* but with some evidence in *P*. This is apparently caused by the reduced *P* velocity along the edges of the superplume (Figure 8) and the fine structure variation along the bottom. In the second step, the output of the MPD is cross correlated with the synthetics (data) in Figure 9a to determine Δ_T (Figure 10c). There appears to be very little variation in Δ_T for *P* waves whereas the *S* variation is more apparent especially for the narrow downwelling zone. Even though these features are complicated, they are likely to be simplified compared to the real African superplume. However, we can examine existing array data searching for diagnostic patterns as predicted above.

3. Application

[14] Although there are many complex record sections sampling the edges of the African superplume, we have chosen data from events A and B discussed earlier that display particularly interesting features to demonstrate the usefulness of the MPD processing. The geometry is displayed in Figure 1 where the great circle paths are arriving at the array sampling the superplume beneath the Indian Ocean.

3.1. Northern Edge (Event A)

[15] We first determine or define an empirical source function, $S(t)$, which is the simplest waveform or wave train in the array, as found from a cross-correlation search. Next, we generate a synthetic for a reference model (such as PREM) using this $S(t)$ as $\dot{D}(t)$ in equation (11) and assume each recording can be modeled by summing $S(t)/2 + S(t + \Delta_{LR})/2$. We define Δ_{LR} as the time separation which refers to the lag of the right half of the Fresnel Zone relative to the left, or split time as discussed above. The data and simulation are given in Figure 11a, where the multipathing is recovered. Next, we correlate the simulated trace (MPD) with observations to determine Δ_T as in the numerical tests. The shifts

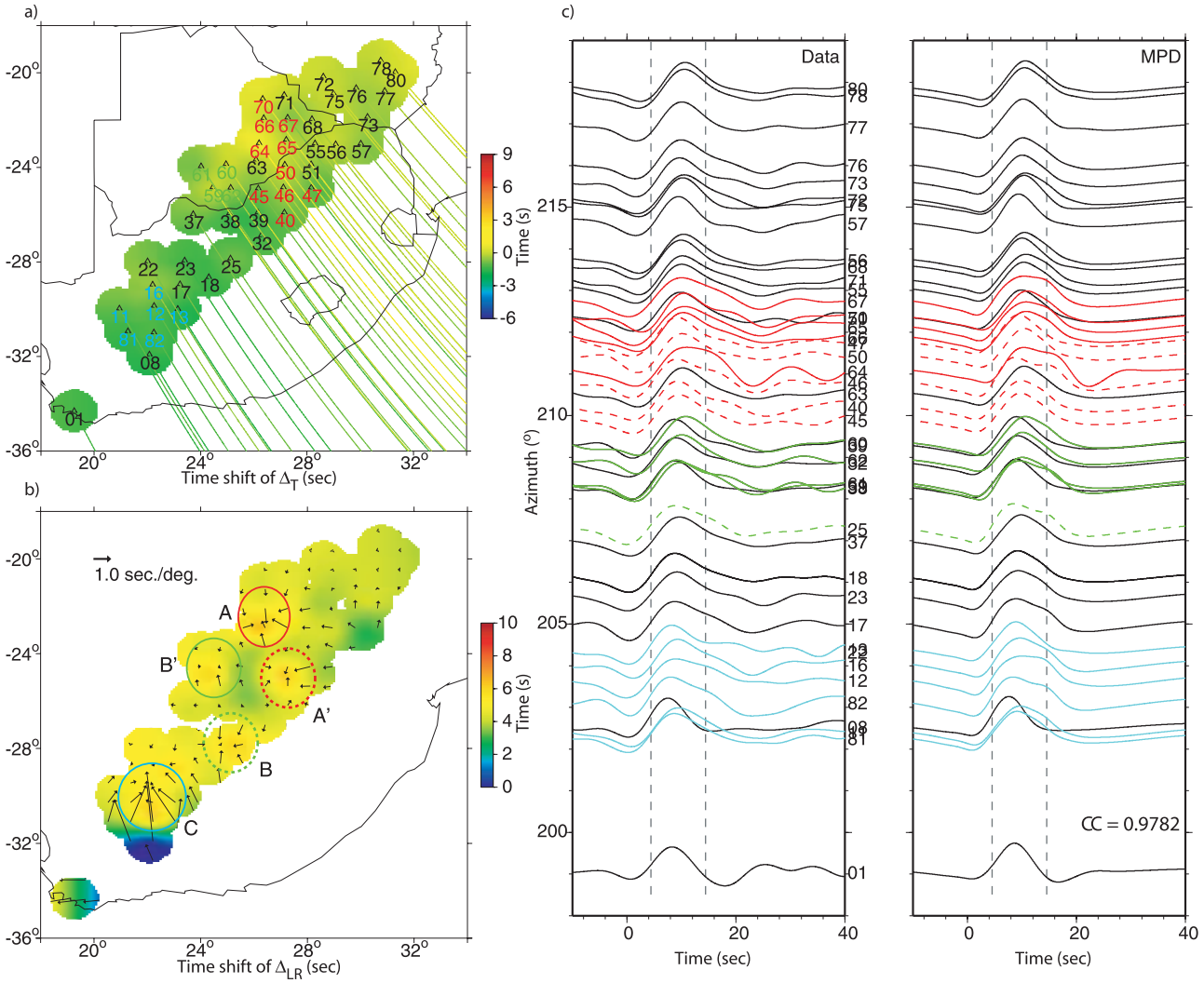

Figure 14. (a, b) Delay time results for P_d (event C). (c) Comparison of P_d observations and MPD simulations. Note that the strong wall signature apparent in *S* results (Figure 13) is nearly absent in *P* results. Some local or small-scale features with circular patterns are displayed at positions A (relatively strong in red), B (weak in blue dashed), and C, near the southern edge of the array. We have included some timing lines to help identify a small delay at the top, which is seen in Figure 14a as a slight change in color.

required in these analyses are given in Figure 11b along with individual raypaths and their associated time delays. The top map displays the overall travel time delays showing the slowdown of the wavefront as it samples the boundary. Note that these plots are independent of how the original data were plotted as in Figure 1. The multipathing shifts, Δ_{LR}, are given in the bottom map of Figure 11b and produce a rather simple picture from northeast to southwest.

[16] A more complete picture is obtained by plotting the gradient (Figure 11c). This pattern is more complex with some patches showing strong out-of-plane effects (longest arrows) perpendicular with the radial direction and some indicating in-plane effects. It appears the wall was never actually crossed or perhaps there are two steps with one associated with the green to pink zone and another to the north. Such complexity in two dimensions has been addressed by *Wang and Wen* [2007]. However, the *P* wave data show little signs of multipathing as discussed earlier, with some complexity given in Figure 11d that looks more like small ULVZs. The southern edge displays more *P* wave distortions as discussed next.

3.2. Southern Edge (Event C)

[17] The waveform data are presented in three frequency bands as given in Figures 12a–12c as broadband low pass, filtered to 5 and 10 s. The upper traces and bottom traces have relatively simple waveforms but are offset by about 15 s, representing the anomalous *S*-velocity structure. The edge is well sampled between 215° and 210°, with a small diffraction wing indicated by a dotted line. Note that at long periods, the edge becomes less obvious as expected; however, the MPD still measures the pulse broadening as displayed in Figures 12d–12f. We have included the cross-correlation (cc) values averaged over the complete profiles, which become slightly higher as the short periods are removed, although the fits are excellent.

[18] In the broadband waveforms (Figures 12a and 12d), the source duration is short enough to allow the O_D operators to be distinct near 213° in azimuths producing multiple peaks. These features are not observed when filtered to longer periods. However, the characteristics of the multipathing delays are generally maintained as demonstrated in Figure 13. Here we display the results in three columns, indicating that the delays of Δ_T are nearly the same (Figures 13a–13c). The gradient results are presented in Figures 13d–13f, where the data showing the strongest azimuthal features remain clear at all frequencies. Note the reversal in arrows near the top of the maps. On the basis of the training exercises, we interpret this as a wall crossing with nearly all of the variation being in azimuth. The multipathing arrows flip sign uniformly along the zero line with stations to the north pointing south, while stations to the south point in a northerly direction. The strength of this multipathing requires a segment of the structure to be nearly aligned with the raypaths such that paths to the south are about 8 s faster than to the north. Note the gradients are large, over 2 s/deg. Some smaller features can be seen in the broadband results labeled A, B, and C. In these images, the multipathing is in both azimuthal and radial directions and appears to be small in dimension. Perhaps, this small structure along the edge is of the type presented in the metastable model, associated with upwelling. The other two zones are more difficult to interpret but could be similar to the small-scale structures farther to the south.

[19] The above small-scale anomalies appear to be also observed in the *P* wave analysis as presented in Figure 14. The data are plotted relative to PREM, and a small timing shift with distance is apparent, with the traces near the bottom arriving slightly early. This feature can be seen in the Δ_T results indicating about a 1.5 s delay. These smaller-scale features occur in both azimuth and distance, which is more indicative of a D″ feature, perhaps associated with ultralow velocity zones near the superplume edges. Unfortunately, the *P* waves contain considerable noise, which means more events need to be analyzed to confirm the existence of these small-scale features. In contrast, there appears to be little evidence for the wall-defining features in *P*, a result compatible with the metastable superplume interpretation discussed earlier.

4. Discussion

[20] Travel time tomography has been one of the main tools in studying Earth structure. Standard practices for geodynamists are to convert these velocity anomalies into density and temperature and infer geophysical observables such as topography and gravity. However, tomographic models produced by smooth, damper inversions underestimate the sharpness of structures. To emphasis this point, we have generated 3-D synthetics (Figure 15) for event A, assuming the well-developed model by *Ritsema et al.* [1999]. Generally only sparse stations are used in such tomographic studies and time delays are minimized by adjusting locations and origin times. The array data, especially at the shorter periods, indicate the sharpness of such structures that are generally missed in long-period studies. Fortunately, these tomographic studies do explain some of the delays and provide crucial information about the geometry of the structure causing these waveform distortions. Simply enhancing the velocity anomalies and adding sharpness has been proven quite useful in generating models that predict improved synthetics fit to data for both regional data, [i.e., *Song and Helmberger*, 2007] and lower mantle data [*Helmberger and Ni*, 2005b]. Another recent approach followed by *Ritsema et al.* [2007] is to examine a large class of models that satisfy the tomographic data but explain additional constraints. DWKM synthetics could then be generated and compared with data directly or use MPD to test for significance of sharp features. In this study, we have provided a new tool for examining the wavefield and providing guidance in how best to approach modification of tomographic results in terms of vertical versus horizontal structure. Instead of forcing array data to produce pulses that cross correlate well enough to obtain accurate travel time picks, we suggest using the broadband wavefield to derive additional MPD-type parameters. From the footprint and timing gradient analysis for a single phase from a single event, we can only determine how sharp the anomaly it is and the orientation of the anomaly. To get exact location and size of the sharp anomaly, we need to combine the MPD parameters derived from different phases and different events. Using different phases for the same event, we can make some decision with respect to what features in the Earth are causing the multipathing effects. As discussed by *Song and Helmberger* [2007], shallow structure in the upper mantle tends to disturb all phases from a particular azimuth, including *P*, *PP*, *S*, and *SS*, etc. If all the phases have strong multipathing effects, the sharp anomaly should exist at shallow depth, which affects all phases by the same degree. If strong multipathing only appears on those phases sampling the deep mantle (*ScS*, *PcP*), we can estimate that the origin of the anomaly is coming from the lower mantle. The rays from different events sample the sharp anomaly differently and generate different MPD patterns. Those patterns can be migrated to different depths and find the coherent parts, which give the sharp boundary laterally. By connecting those boundaries at different depth, we can construct a 3-D image of the sharp edges. Equation (7) shows that the radius of lit region changes with the depth of reference plane. The deeper the reference plane, the wider the lit region. For an event station couple, a migrated Δ_{LR} image at certain depth is a circle centered at the ray piercing point at that depth with radius Δ_l. The value along the circle is Δ_{LR}. The summation of all migrated images for every event station couple will give a strong indication of sharp boundary if it arises at that depth. This technique is similar to that used in the finite-frequency tomography using adjoint methods, which the summation of finite-frequency sensitivity kernels defines the overall misfit kernel [*Tape et al.*, 2007]. We will discuss this migration method in future efforts.

[21] Since temperature and chemistry affect the *P* and *S* velocities differently, studying *P* and *S* waveforms from the same events can provide unique detail into differential measures; that is, $R = dlnV_s/dlnV_p$. This parameter is important in understanding the mineral physics in the deep mantle [*Masters et al.*, 2000]. An approximate value for *R* is $(V_s\delta t_s/V_p\delta t_p)$, where δt_s and δt_p are travel time perturbations [*Souriau and Woodhouse*, 1985]. Accurate estimates of the δt_s and δt_p are obtained from applying the above operators as displayed in Figure 14 for event C. In this case, the *R*

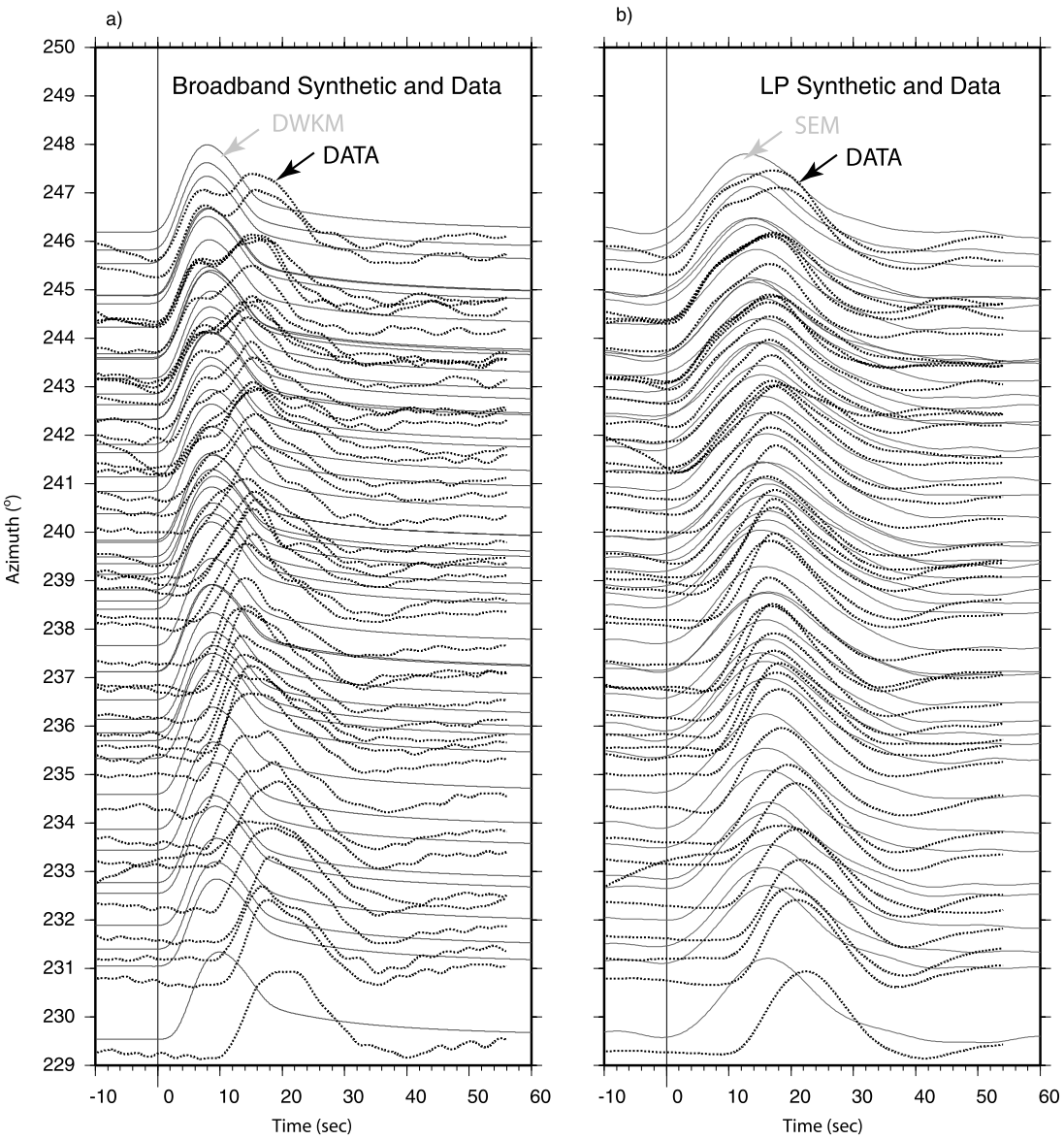

Figure 15. Direct comparison of synthetic predictions (solid lines) from Ritsema's tomographic model [*Ritsema et al.*, 1999] with observations (dotted lines). (a) Observations plotted in azimuth for event A against DWKM synthetics (broadband). (b) Long-period (LP) synthetics filtered to 18 s generated by SEM with data. The synthetics show less than 4 s delays, which is too small to satisfy the data. Tomography models are generally too smooth to predict the multipathing observed here.

factor is quite high ($R > 6$) because the P waves show very little change across the superplume boundary. Generally, the P waves encounter some delays when crossing the edges as discussed earlier, and the average value found by *Masters et al.* [2000] of 3.8 for the Pacific and South African structures appears to be generally compatible with our results, which are somewhat higher. To estimate R, we average over samples inside the superplume (top seven stations in Figure 13) for S waves and for P waves (Figure 14), where we normalize the Δ_T to the region most like PREM (bottom six stations in Figure 13). Then

$$R = \frac{1}{n}\sum_{i=1}^{n}\frac{V_S \Delta_T^i(S)}{V_P \Delta_T^i(P)}, \tag{12}$$

which yields R of about 5.5. Such a high value is compatible with the metastable model that was designed for this ratio. Note there is a whole family of $\Delta\rho$ and K_s that will yield metastable superplumes [*Tan and Gurnis*, 2005], and resolving this number is essential in defining possible mineralogy.

[22] Another measure of rapid changes in material properties is to use the shift, or Lateral Gradient Coefficient (LGC),

$$LGC = \frac{1}{n}\sum_{i=1}^{n}\frac{V_S \Delta_{LR}^i(S)}{V_P \Delta_{LR}^i(P)}, \tag{13}$$

or perhaps their derivatives with represent to azimuth as displayed in Figure 10. Sharp changes in temperature

usually yield similar changes in *P* and *S* velocities while chemistry is more effective in producing large coefficients. Averaging over the length of arrows in Figures 13 and 14 for the same set of stations produces estimates greater than 8, where the *P* waves are probably near the noise level. The arrow lengths in Figures 13a and 13d suggest azimuthal jumps of over 2 s/deg, which agree with those produced by the metastable model presented in Figure 10. We have not been able to explain such significant lateral gradients without introducing a wall, which is difficult to detect at periods greater than 20 s. In short, there appears a number of ways to quantify the obvious complexity introduced in Figure 1. Some small-scale features, especially prominent in the *P* results given in Figure 14, appear to be associated with structure inside the superplume. More data need to be processed to establish such detail since other small-scale structures probably exist elsewhere in the Earth.

[23] In summary, we have introduced a new method of processing array data which will make it easier to identify structural boundaries and sharpen tomographic images. The method decomposes observed pulses embedded in body wave observations and uses the relative timing of these array arrivals to identify in-the-plane versus out-of-plane multipathing. Preliminary results for a few events observed by the South African Kaapvaal array reveal strong evidence of 3-D wave propagation and the fine-scale nature of boundaries.

[24] **Acknowledgments.** We would like to thank two reviewers and the Associate Editor. Their suggestions and comments were greatly appreciated and made significant improvements to the manuscript. We also thank Tarje Nissen-Meyer for helpful discussions. Data were provided by IRIS data centers. All maps in this paper were produced using GMT developed by Paul Wessel and Walter H. F. Smith. This work was supported by National Science Foundation grants NSF-EAR0636012. Contribution 10014 of the Division of Geological and Planetary Sciences, California Institute of Technology.

References

Aki, K., and P. G. Richards (2002), *Quantitative Seismology*, 2nd ed., 700 pp., Univ. Sci., Sausalito, Calif.

Anderson, D. L. (2002), The case for irreversible chemical stratification of the mantle, *Int. Geol. Rev.*, *44*, 97–116, doi:10.2747/0020-6814.44.2.97.

Bunge, H.-P., C. R. Hagelberg, and B. J. Travis (2003), Mantle circulation models with variational data assimilation: Inferring past mantle flow and structure from plate motions histories and seismic tomography, *Geophys. J. Int.*, *152*, 280–301, doi:10.1046/j.1365-246X.2003.01823.x.

Chapman, C. H. (1976), Exact and approximate generalized ray theory in vertically inhomogeneous media, *Geophys. J. R. Astron. Soc.*, *46*, 201–233.

Chapman, C. H. (2004), *Fundamentals of Seismic Wave Propagation*, 632 pp., Cambridge Univ. Press, New York.

Davaille, A. (1999), Simultaneous generation of hotspots and superswells by convection in a heterogeneous planetary mantle, *Nature*, *402*, 756–760, doi:10.1038/45461.

Dziewonski, A. M., and D. L. Anderson (1981), Preliminary Reference Earth Model, *Phys. Earth Planet. Inter.*, *25*, 297–356, doi:10.1016/0031-9201(81)90046-7.

Gilbert, F., and D. V. Helmberger (1972), Generalized ray theory for a layered sphere, *Geophys. J. R. Astron. Soc.*, *27*, 57–80.

Gonnermann, H. M., M. Manga, and A. M. Jellinek (2002), Dynamics and longevity of an initially stratified mantle, *Geophys. Res. Lett.*, *29*(10), 1399, doi:10.1029/2002GL014851.

Grand, S., and D. V. Helmberger (1984), Upper mantle shear structure of North America, *Geophys. J. R. Astron. Soc.*, *76*, 399–438.

Gurnis, M., M. E. Wysession, E. Knittle, and B. A. Buffet (Eds.) (1998), *The Core-Mantle Boundary Region*, *Geodyn. Ser.*, vol. 28, 334 pp., AGU, Washington, D. C.

Hansen, U., and D. A. Yuen (1989), Dynamical influences from thermal-chemical instabilities at the core-mantle boundary, *Geophys. Res. Lett.*, *16*, 629–632, doi:10.1029/GL016i007p00629.

Helmberger, D. V., and S. Ni (2005a), Seismic modeling constraints on the South African super plume, in *Earth's Deep Mantle: Structure, Composition, and Evolution*, *Geophys. Monogr. Ser.*, vol. 160, edited by R. D. van der Hilst et al., pp. 63–81, AGU, Washington, D. C.

Helmberger, D. V., and S. Ni (2005b), Approximate 3D bodywave synthetics for tomographic models, *Bull. Seismol. Soc. Am.*, *95*(1), 212–224, doi:10.1785/0120040004.

James, D. E., M. J. Fouch, J. C. VanDecar, S. van der Lee, and Kaapvaal Seismic Group (2001), Tectospheric structure beneath southern Africa, *Geophys. Res. Lett.*, *28*, 2485–2488, doi:10.1029/2000GL012578.

Kellogg, L., B. H. Hager, and R. D. van der Hilst (1999), Compositional stratification in the deep mantle, *Science*, *283*, 1881–1884, doi:10.1126/science.283.5409.1881.

Komatitsch, D., and J. Tromp (2002a), Spectral-element simulations of global seismic wave propagation: I. Validation, *Geophys. J. Int.*, *149*, 390–412, doi:10.1046/j.1365-246X.2002.01653.x.

Komatitsch, D., and J. Tromp (2002b), Spectral-element simulations of global seismic wave propagation: II. 3D models, oceans, rotation, and gravity, *Geophys. J. Int.*, *150*, 303–318, doi:10.1046/j.1365-246X.2002.01716.x.

Masters, G., G. Laske, H. Bolton, and A. M. Dziewonski (2000), The relative behavior of shear velocity, bulk sound speed, and compressional velocity in the mantle: Implications for chemical and thermal structure, in *Earth's Deep Interior: Mineral Physics and Tomography From the Atomic to the Global Scale*, *Geophys. Monogr. Ser.*, vol. 117, edited by S. Karato et al., pp. 63–87, AGU, Washington, D. C.

McNamara, A. K., and S. Zhong (2004), Thermochemical structures within a spherical mantle: Superplumes or piles?, *J. Geophys. Res.*, *109*, B07402, doi:10.1029/2003JB002847.

Ni, S., and D. V. Helmberger (2003a), Seismological constraints on the South African superplume: Could be the oldest distinct structure on Earth, *Earth Planet. Sci. Lett.*, *206*, 119–131, doi:10.1016/S0012-821X(02)01072-5.

Ni, S., and D. V. Helmberger (2003b), Ridge-like lower mantle structure beneath South Africa, *J. Geophys. Res.*, *108*(B2), 2094, doi:10.1029/2001JB001545.

Ni, S., and D. V. Helmberger (2003c), Further constraints on the African superplume structure, *Phys. Earth Planet. Inter.*, *140*, 243–251, doi:10.1016/j.pepi.2003.07.011.

Ni, S., D. V. Helmberger, and J. Tromp (2005), 3D structure of the African super plume from waveform modeling, *Geophys. J. Int.*, *161*, 283–294, doi:10.1111/j.1365-246X.2005.02508.x.

Ritsema, J., H. J. van Heijst, and J. H. Woodhouse (1999), Complex shear wave velocity structure imaged beneath Africa and Iceland, *Science*, *286*, 1925–1928, doi:10.1126/science.286.5446.1925.

Ritsema, J., A. K. McNamara, and A. L. Bull (2007), Tomographic filtering of geodynamic models: Implications for model interpretation and large-scale mantle structure, *J. Geophys. Res.*, *112*, B01303, doi:10.1029/2006JB004566.

Scott, P., and D. V. Helmberger (1985), Applications of the transmitted Kirchhoff-Holmholtz method to transmitted body waves and possible structural effects at NTS, *Bull. Seismol. Soc. Am.*, *75*, 131–156.

Shearer, P. (1993), Global mapping of upper mantle reflectors from long-period SS precursors, *Geophys. J. Int.*, *115*, 878–904, doi:10.1111/j.1365-246X.1993.tb01499.x.

Song, T. R., and D. V. Helmberger (2007), Validating tomographic model with broadband waveform modeling: An example from the LA RISTRA transect in the southwestern United States, *Geophys. J. Int.*, *171*, 244–258, doi:10.1111/j.1365-246X.2007.03508.x.

Souriau, A., and J. H. Woodhouse (1985), A worldwide comparison of predicted S-wave delays from a three-dimensional upper mantle model with P wave station corrections, *Phys. Earth Planet. Inter.*, *39*, 75–88, doi:10.1016/0031-9201(85)90075-5.

Sun, D., E. Tan, D. V. Helmberger, and M. Gurnis (2007), Seismological support for the metastable superplume model, sharp features, and phase changes, within the lower mantle, *Proc. Natl. Acad. Sci. U. S. A.*, *104*(22), 9151–9155, doi:10.1073/pnas.0608160104.

Tackley, P. (2000), Mantle convection and plate tectonics: Toward an integrated physical and chemical theory, *Science*, *288*, 2002–2007, doi:10.1126/science.288.5473.2002.

Tan, E., and M. Gurnis (2005), Metastable superplumes and mantle compressibility, *Geophys. Res. Lett.*, *32*, L20307, doi:10.1029/2005GL024190.

Tan, E., and M. Gurnis (2007), Compressible thermochemical convection and application to lower mantle structures, *J. Geophys. Res.*, *112*, B06304, doi:10.1029/2006JB004505.

Tape, C., Q. Liu, and J. Tromp (2007), Finite-frequency tomography using adjoint methods: Methodology and examples using membrane surface waves, *Geophys. J. Int.*, *168*, 1105–1129, doi:10.1111/j.1365-246X.2006.03191.x.

Wang, Y., and L. Wen (2007), Geometry and P and S velocity structure of the "African Anomaly", *J. Geophys. Res.*, *112*, B05313, doi:10.1029/2006JB004483.

Wen, L. (2001), Seismic evidence for a rapidly varying compositional anomaly at the base of the Earth's mantle beneath the Indian Ocean, *Earth Planet. Sci. Lett.*, *194*, 83–95, doi:10.1016/S0012-821X(01)00550-7.

Zhu, L., and D. V. Helmberger (1998), Moho offset across the northern margin of the Tibetan Plateau, *Science*, *281*, 1170–1172, doi:10.1126/science.281.5380.1170.

D. Bower, D. Helmberger, and D. Sun, Seismological Laboratory, 252-21, California Institute of Technology, Pasadena, CA 91125, USA. (sdy@gps.caltech.edu)

S. Ni, URS, Inc., 566 El Dorado Street, Pasadena, CA 91101, USA.